The International Journal of Advanced Manufacturing Technology
https://doi.org/10.1007/s00170-018-03280-y

ORIGINAL ARTICLE

# Trochoidal milling: investigation of dynamic stability and time domain simulation in an alternative path planning strategy

Farbod Akhavan Niaki[1] · Abram Pleta[1] · Laine Mears[1] · Nils Potthoff[2] · Jim A. Bergmann[2] · Petra Wiederkehr[2]

Received: 2 August 2018 / Accepted: 28 December 2018


## Abstract

Trochoidal milling is an alternative path planning strategy with the potential of increasing material removal rate per unit of tool wear and therefore productivity cost while reducing cutting energy and improving tool performance. These characteristics in addition to low radial immersion of the tool make trochoidal milling a desirable tool path in machining difficult-to-cut alloys such as nickel-based superalloys. The objective of this work is to study the dynamic stability of trochoidal milling and investigate the interaction of tool path parameters with stability behavior when machining IN718 superalloy. While there exist a few published works on dynamics of circular milling (an approximated tool path for trochoidal milling), this work addresses the dynamics of the actual trochoidal tool path. First, the chip geometry quantification strategy is explained, then the chatter characteristic equation in trochoidal milling is formulated, and chatter stability lobes are generated. It is shown that unlike a conventional end-milling operation where the geometry of chips remains constant during the cut (resulting in a single chatter diagram representing the stability region), trochoidal milling chatter diagrams evolve in time with the change in geometry (plus cutter entering and exiting angles) of each chip. The limit of the critical depth of cut is compared with conventional end milling and shown that the depth of cut can be increased up to ten times while preserving stability. Finally, the displacement response of the cutting tool is simulated in the time domain for stable and unstable cutting regions; numerical simulation and theoretical results are compared.

**Keywords** Trochoidal milling · Dynamic stability · Superalloys · IN718

✉ Farbod Akhavan Niaki
fakhava@clemson.edu

Abram Pleta
apleta@clemson.edu

Laine Mears
mears@clemson.edu

Nils Potthoff
potthoff@isf.maschinenbau.uni-dortmund.de

Jim A. Bergmann
jim.bergmann@tu-dortmund.de

Petra Wiederkehr
petra.wiederkehr@tu-dortmund.de

[1] International Center for Automotive Research, Clemson University, Greenville, SC, USA

[2] LS14, Virtual Machining, TU Dortmund University, Dortmund, Germany

## 1 Introduction

With rapid advancements in transportation and power generation industries, a demand for advanced nickel-based superalloys is on the rise [1]. High strength and corrosion resistivity of these alloys are the two most important factors that make nickel-based superalloy an excellent candidate for high temperature and pressure environments. However, cutting these alloys is extremely difficult due to their strength and low thermal conductivity which leads to a temperature rise at the tool-workpiece interface and premature failure of the tool due to excessive notch wear [2]. As a result, a significant amount of work is published to address various metallurgical and machinability characteristics of superalloys. The recent articles published by Thakur et al. and Zhu et al. are extensively reviewing those aspects [2, 3]. Within the past decade, the emergence of low-cost sensing technologies and availability of machine data through open-source standards such as MTConnect have opened new doors for affordable monitoring

Published online: 07 January 2019

strategies outside of research laboratories with high technology readiness level. In superalloy machining, monitoring the state of the machining operation becomes critical due to high cost of material and tooling. An unexpected tool failure results in re-work or scrapping of the workpiece and therefore revenue loss. Deterministic-based monitoring strategies such as neural network [4, 5], or support vector machine [6, 7] and stochastic-based monitoring such as Kalman and particle filters [8–10], hidden Markov models [11], or random forest [12] for tool wear monitoring (specifically tool flank wear) have shown degrees of success by various researchers. Even though there is a significant body of work on monitoring strategies, one specific alternative solution for improving machining productivity is left out by many researchers. Cutting strategies such as circular or trochoidal milling are alternative path planning solutions that have been recently introduced into CAM software packages. Pleta et al. demonstrated that using a trochoidal milling strategy, it is possible to achieve up to 600% increase in material removed per unit of tool wear in comparison with a similar end-milling strategy in cutting IN738 superalloy, which shows the significance of this alternative cutting strategy to increase productivity [13].

In general, trochoidal milling can be studied in four steps, shown as a knowledge tree in Fig. 1. The first step is chip thickness and force modeling. Kardes and Altintas [14] as well as Otkur and Lazoglu [15] were the first to introduce a model of chip thickness for trochoidal milling. However, their modeling strategy is a simplified trochoidal tool path estimation which considers circular motion of the tool center independent of a secondary step in feed direction. In contrast, the actual trochoidal tool path is a superposition of tool circular and translational motions in the feed direction (to avoid confusion, the term "circular milling" is used in this article to distinguish the simplified tool path). Deng et al. used the same formulation and studied circular tool path in corner machining [16]. The relation between material removal rate and machining time with respect to cutting force were investigated and optimal parameter selection strategy was laid out. In [17], a new chip thickness model based on numerical intersection-finding algorithm was proposed for the actual trochoidal path which was shown to be capable of generating the exact uncut chip geometry. The simulated and experimental forces were compared, and corresponding error was quantified.

The second step in studying trochoidal milling is stability prediction and chatter analysis. To the best of authors' knowledge only two articles have discussed this matter, and only for the simpler circular milling case. In [14], two methods of frequency domain solution and time finite element analysis were used to create the stability lobe diagram of circular milling; stable and unstable regions were identified. The same approach was taken by Yan et al. in circular milling of steel alloy as well [18]. Tool path planning and NC programming is the next step in the knowledge tree of trochoidal milling. Optimization of trochoidal parameters to improve machining time and productivity was studied by Rouch et al. [19]. In [20, 21], the effect of trochoidal path parameters on tool life and forces were studied in high speed operations. The energy demand, effective cutting time and material removal rate in conventional milling was compared with trochoidal milling in [22] and it was shown that higher material removal rate is achievable in trochoidal milling with the cost of higher power consumption. Finally, the last portion of the trochoidal knowledge tree is the degree of effect on the machining affected zone which is one of the most important aspects governing the resultant workpiece life behavior. From the industrial standpoint, trochoidal milling allows for low radial immersion and high axial depth of cut in cutting. The low radial immersion can cause an increase in temperature due to plowing effect of the tool on the surface of the workpiece and high axial depth of cut can induce excessive residual stress beneath the surface. Since this alternative tool path is used for cutting difficult-to-machine materials, such as nickel-based superalloys or titanium-based alloys, it is very important to be able to quantify the degree of microstructural damage in both radial and axial directions and to investigate the machining affected zone region. While, there are limited attempts to study the first

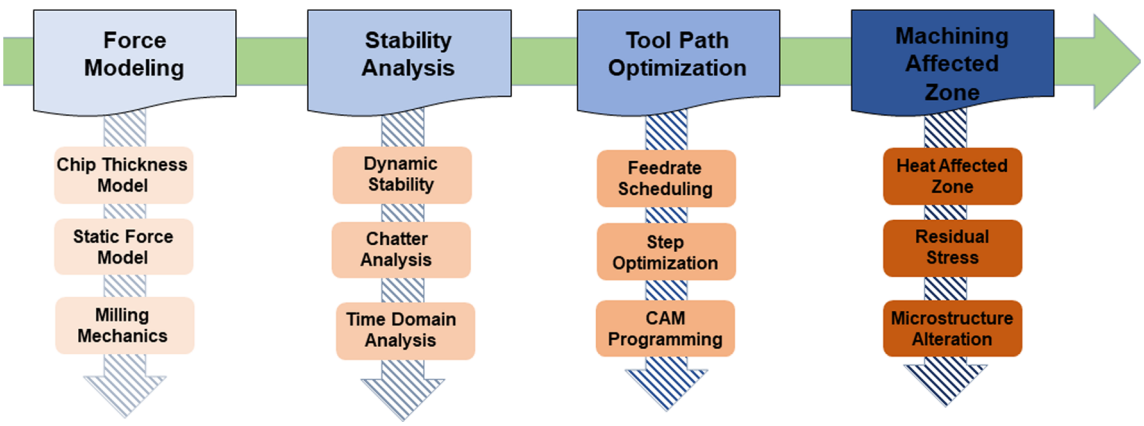


**Fig. 1** Knowledge tree in trochoidal milling

three aspects in trochoidal knowledge tree of Fig. 1, the effect of tool path on machining affected area is left blank so far.

As it was explained in the literature review, there are only few articles [14–16] that proposed a methodology for mechanics of trochoidal milling (i.e., chip thickness and force modeling). All these articles simplified the trochoidal tool path to circular tool path and therefore their solution is an approximation. In the previous work of the authors [17], the methodology for constructing the exact chip geometry was provided and static force was simulated with consideration of infinite rigidity of the tool. In this work, the infinite rigidity assumption of the cutting tool will be removed and cutting dynamics of the operation will be studied. Therefore, the objective of this work is to study the dynamic stability and vibrational response of the cutting tool in the actual trochoidal tool path. Furthermore, the workpiece material is chosen as IN718 to purposefully showcase the application and proper trochoidal path parameter selection suitable for difficult-to-machine superalloys. The organization of this work is as follows: the chip thickness formulation for chatter stability prediction and time domain simulation of trochoidal milling are discussed in Section 2. In Section 3, the experimental setup for system identification and design of experiment is given. Results and comparison of stability lobe diagrams in trochoidal milling and conventional end-milling is discussed in Section 4, followed by a time domain study of cutting tool vibration. Finally, the conclusion and future directions of the work is given in Section 5.

## 2 Theoretical background

### 2.1 Trochoidal tool path and chip formation

The trochoidal tool path can be expressed by three main parameters, namely: rotation rate (i.e., spindle rpm denoted as $\dot{\theta}$), nutation rate (denoted as $\dot{\phi}$), and step-over feed rate (denoted as $v$). The trajectorial motion of the tool tip in $x$- and $y$-directions is given by Eqs. 1 and 2, where $R_{cp}$ is the radius of tool center, $R_d$ is radius of the cutting tool, and $t$ is time. Unlike conventional up- (or down-)milling, where the chip geometry profile remains constant during the cut, in trochoidal milling, chip geometry changes over the nutation cycle. This is shown in Fig. 2 where the chip geometry at the start, middle, and end of a nutation in trochoidal milling is compared with slot milling.

$$X_t = R_{cp}\cos\left(\dot{\phi}t\right) + R_t\cos\left(-\frac{2\pi}{60}\dot{\theta}t\right) \tag{1}$$

$$Y_t = R_{cp}\sin\left(\dot{\phi}t\right) + R_t\sin\left(-\frac{2\pi}{60}\dot{\theta}t\right) + vt \tag{2}$$

Contrary to conventional milling, where chip thickness, denoted as $h(t)$ in Fig. 2b, can be approximated with a closed form solution, in trochoidal milling, a closed form solution to represent chip geometries cannot be directly calculated. As a result, numerical approximation techniques must be utilized to calculate the chip thickness. The authors previously published an article detailing a method of finding chip thickness in trochoidal milling through a numerical intersection method [17]. In that work, a detailed algorithm was discussed for single- and multi-tooth cutters. Therefore, the chip thickness derivation will not be discussed to avoid duplicity and results (i.e., calculated uncut chip thickness, corresponding simulated tangential, and radial forces) will be shown without proof. Assuming a positive direction convention for forces in Cartesian and polar coordinates is shown in Fig. 3, uncut chip thickness and cutting force evolution over time can be found (see [17] for details).

Simulated cutting forces in Fig. 3c were derived with an assumption of rigid tool (i.e., no vibrational effect). As shown in Eq. 3, tangential force (denoted as $F_T$) and radial force (denoted as $F_R$) are the product of chip area and tangential and normal cutting pressure coefficients denoted as $K_T$ and $K_R$ respectively. Utilizing the rotation matrix $R$ shown in Eq. 4, the tangential and radial forces can be projected into $x$- and $y$-directions. Note that, the parameter $b$ in Eq. 3 represents axial depth of cut and $K_{te}$ and $K_{re}$ are edge coefficients representing the frictional force due to tool wear.

$$\begin{aligned} F_T &= K_T bh + K_{te} b \\ F_R &= K_R bh + K_{re} b \end{aligned} \tag{3}$$

$$\begin{aligned} \left[F_X \quad F_Y\right]^T &= R\left[F_T \quad F_R\right]^T \quad , \quad R \\ &= \begin{bmatrix} -\sin(\theta) & -\cos(\theta) \\ -\cos(\theta) & \sin(\theta) \end{bmatrix} \end{aligned} \tag{4}$$

### 2.2 Fourier series approach for dynamic stability analysis in trochoidal milling

Altintas and Budak [23] developed a method for dynamic stability prediction in milling based on Fourier series approach. The method described in [23] targeted the conventional slot-milling operation where same chip geometry is created per tool rotation. As shown in Fig. 2b, in slot milling, the cutter entering and exiting angles remain constant per chip. In trochoidal tool path however, the entering and existing angles of the tool are constantly changing per chip and therefore, the resultant formulation proposed in [23] cannot be used directly.

Considering a non-rigid tool, the instantaneous chip thickness $h$ for a given chip $\{N\}$ can be written as Eq. 5, where $h_{\text{nom}}$ is the nominal uncut chip thickness (derived using numerical algorithm described in [17]), $R_{\text{prev}}$ is the vibrational contribution of previous cutter or previous nutation on the given chip, $R_{\text{curr}}$ is the vibrational contribution of the current cutter on the given chip, and $g(\theta)$ is a switching function with its value equal to unity when the cutter is engaged in the cut.

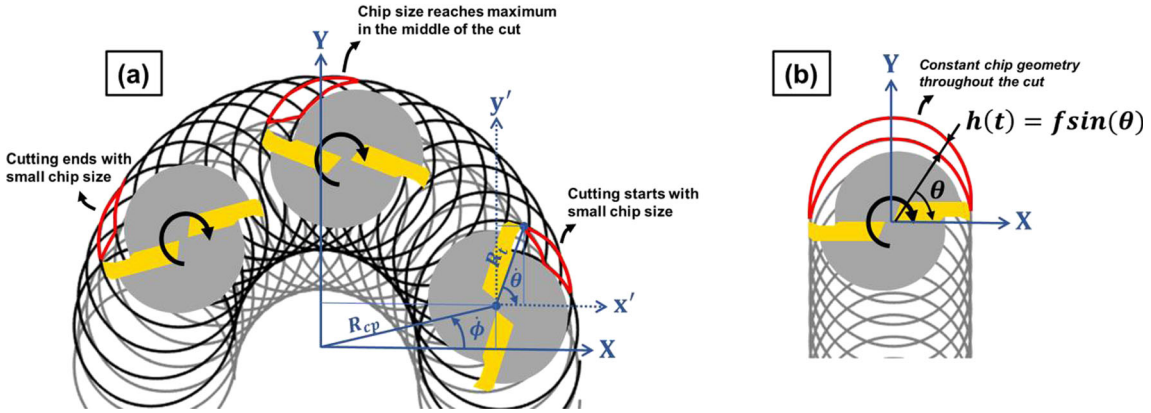


**Fig. 2** Geometrical chip shape representation for (**a**) trochoidal milling, and (**b**) conventional end milling

Considering negligible frictional effect on the flank face of the tool (i.e., $K_{re} = K_{te} = 0$), Eq. 5 is substituted in Eq. 3 to obtain dynamic cutting forces in $x$- and $y$-directions and is shown in Eq. 6 (see Appendix B for mathematical derivation). Note that the positive direction of forces in $x$- and $y$- and normal to the surface are shown in Fig. 3a.

$$h^{\{N\}}(\theta) = \left(h_{\text{nom}}^{\{N\}} - R_{\text{prev}} + R_{\text{curr}}\right) g(\theta) \tag{5}$$

$$\begin{bmatrix} F_X \\ F_Y \end{bmatrix} = \frac{1}{2} b K_T [A] \begin{bmatrix} \Delta x \\ \Delta y \end{bmatrix} \tag{6}$$

In Eq. 6, matrix $A$ is known as the time-dependent force coefficient matrix which depends on chip entering and exiting angles and is calculated as in Eq. 7. Here, parameter $\gamma$ represents the ratio of radial to tangential cutting pressure coefficients ($=K_R/K_T$), $\theta_i$ is the instantaneous cutter angle which is a function of time and $N_t$ is the number of cutting edges. To remove the time dependency from matrix $A$, Altintas and Budak first suggested to take a Fourier transform from $A$ and then keep the constant Fourier coefficient as an approximation of the original matrix $A$; thus its time-dependency can be eliminated [23]. In Eq. 8, the constant Fourier coefficient of matrix $A$ is given. The integral should be taken over a complete tool rotation. Since in trochoidal milling, the cutter engagement angle varies and is dependent on the chip geometry, the constant $A_c$ in Eq. 8 varies for each chip and needs to be updated per tool nutation angle based on the cutters' entering and existing angles. For instance, for a double-flute cutting tool shown in Fig. 4 (where two chips are produced per one full rotation of the tool), the $A$ matrix should be calculated as in Eq. 9.

$$[A] = \begin{bmatrix} a_{xx} & a_{xy} \\ a_{yx} & a_{yy} \end{bmatrix} = \begin{bmatrix} \sum_{i=1}^{N_t} g(\theta_i)(\sin(2\theta_i) + \gamma(1 + \cos(2\theta_i))) & \sum_{i=1}^{N_t} g(\theta_i)(1 - \cos(2\theta_i) + \gamma\sin(2\theta_i)) \\ \sum_{i=1}^{N_t} g(\theta_i)(1 + \cos(2\theta_i) - \gamma\sin(2\theta_i)) & \sum_{i=1}^{N_t} g(\theta_i)(\sin(2\theta_i) - \gamma(1 - \cos(2\theta_i))) \end{bmatrix} \tag{7}$$

$$[A] \approx [A_c] = \frac{1}{2\pi} \int_0^{2\pi} [A] d\theta = \frac{1}{2\pi} \int_{\theta_{\text{enter}}}^{\theta_{\text{exit}}} [A] d\theta = \begin{bmatrix} ai_{xx} & ai_{xy} \\ ai_{yx} & ai_{yy} \end{bmatrix} \tag{8}$$

Double-flute tool in Fig. 4:

$$[A_c] = \frac{1}{2\pi} \left[ \int_{\theta_{\text{enter\_c2}}}^{\theta_{\text{exit\_c1}}} [A(\theta_{c1})] d\theta_{c1} + \int_{\theta_{\text{enter\_c2}}}^{\theta_{\text{exit\_c2}}} [A(\theta_{c2})] d\theta_{c2} \right] \tag{9}$$

Considering Eq. 10 as the general definition of a frequency response function (FRF), the characteristic

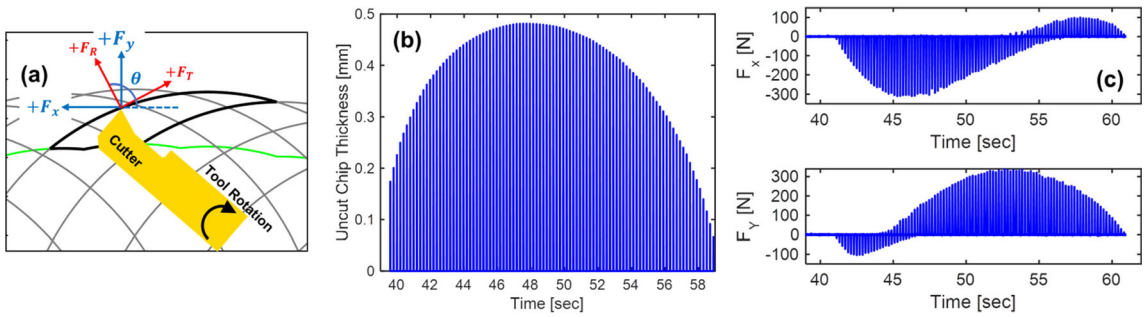


**Fig. 3** Uncut chip thickness (and simulated cutting forces) varies during a nutation in trochoidal milling, (**a**) positive direction convention; (**b**) chip thickness evolution for single flute tool with $\dot{\theta}$ =300 rpm, $\dot{\phi}$ =0.64 rad/s, and $v$ = 0.05 mm/s; and (**c**) simulated cutting forces in $x$- and $y$-directions for axial depth of cut of 0.5 mm

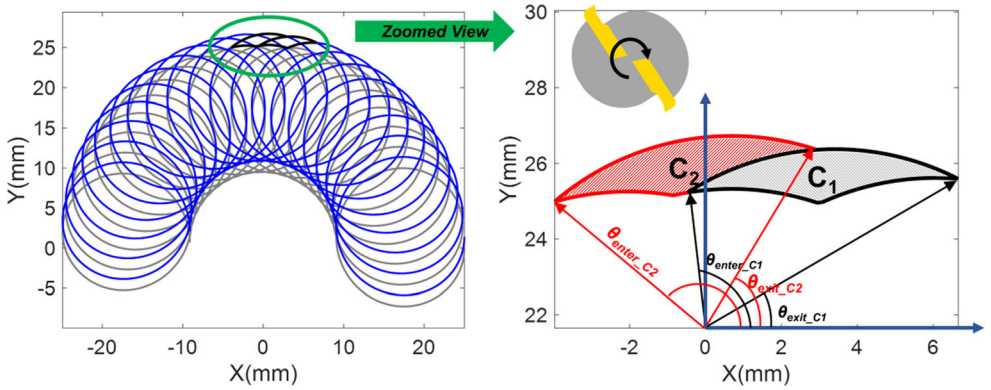


**Fig. 4** Entering and existing angles of the cutter varies over time in trochoidal milling

equation of trochoidal milling dynamics can be derived as in Eq. 11 (see Appendix C for mathematical derivation). In Eq. 10, $[X_{\text{curr}}\ Y_{\text{curr}}]^{\text{T}}$ is the vibration contribution of the current cutter, $[X_{\text{prev}}\ Y_{\text{prev}}]^{\text{T}}$ is the vibration contribution of previous cutter pass, $\tau$ is the tooth passing period, $\omega_c$ is the chatter frequency, and $I$ is the identify matrix. Equation 11 is similar to the characteristic equation of conventional milling given in [23]. However, the matrix $A_c$ needs to be updated based on the chip geometry (i.e., cutter entering and exiting angles).

$$\begin{bmatrix} X_{\text{curr}} \\ Y_{\text{curr}} \end{bmatrix} = \begin{bmatrix} FRF_{XX} & 0 \\ 0 & FRF_{YY} \end{bmatrix} \begin{bmatrix} F_X \\ F_Y \end{bmatrix} e^{-i\omega_c t} \ \text{AND} \ \begin{bmatrix} X_{\text{prev}} \\ Y_{\text{prev}} \end{bmatrix} = \begin{bmatrix} FRF_{XX} & 0 \\ 0 & FRF_{YY} \end{bmatrix} \begin{bmatrix} F_X \\ F_Y \end{bmatrix} e^{-i\omega_c (t-\tau)} \tag{10}$$

$$\det\left( I - \frac{1}{2} b K_T \left(1 - e^{-i\omega_c \tau}\right) [A_c] \begin{bmatrix} FRF_{XX} & 0 \\ 0 & FRF_{YY} \end{bmatrix} \right) = 0 \tag{11}$$

Defining the product of $A_c$ and FRF matrices as $\text{FRF}_{\text{orient}}$, Eq. 11 can be reformulated as Eq. 12. By rewriting the parameter $\lambda$ in Eq. 13 as a complex number and solving for $b$, the axial depth of cut for initiation of chatter can be derived as in Eq. 14. Here, the parameter $\eta$ (given in Eq. 15) is derived based on the assumption that axial depth of cut must be a real number, and therefore the imaginary part ($\lambda_{\text{imag}}$) in Eq. 13 must be zero. The chatter dependent spindle speed ($\varpi$) is calculated similar to conventional milling and is given in Eq. 16, where $n$ is an integer number starting from zero. Combining Eqs. 14 to 16 creates the chatter stability diagram for trochoidal milling.

$$\det(FRF_{\text{orient}} - \lambda I) = 0 \quad , \quad \lambda = \frac{2}{bK_T(1 - e^{-i\omega_c \tau})} \tag{12}$$

$$\lambda = \frac{2}{bK_T(1 - e^{-i\omega_c \tau})} = \lambda_{\text{real}} + i\lambda_{\text{imag}}$$
$$\overset{\text{Solving for } b}{\rightarrow} b = \frac{2}{K_T} \left[ \frac{\lambda_{\text{real}}(1 - \cos(\omega_c \tau)) - \lambda_{\text{imag}} \sin(\omega_c \tau)}{2(1 - \cos(\omega_c \tau))\left(\lambda_{\text{real}}^2 + \lambda_{\text{imag}}^2\right)} + i \frac{\left(-\lambda_{\text{real}} \sin(\omega_c \tau) - \lambda_{\text{imag}}(1 - \cos(\omega_c \tau))\right)}{2(1 - \cos(\omega_c \tau))\left(\lambda_{\text{real}}^2 + \lambda_{\text{imag}}^2\right)} \right] \tag{13}$$

$$b_{\text{lim}} = \frac{\lambda_{\text{real}}(1 + \eta^2)}{K_T\left(\lambda_{\text{real}}^2 + \lambda_{\text{imag}}^2\right)} \tag{14}$$

$$\eta = \frac{\lambda_{\text{imag}}}{\lambda_{\text{real}}} = \frac{\sin(\omega_c \tau)}{-1 + \cos(\omega_c \tau)} \tag{15}$$

$$\varpi = \frac{60\omega_c}{N_t(\pi - 2\tan^{-1}(\eta) + 2\pi n)} \tag{16}$$

## 2.3 Time domain approach for local dynamic stability analysis in trochoidal milling

In addition to chatter stability which provides insight on stable/unstable cutting regions in trochoidal milling, time domain simulation can be utilized to investigate the dynamic behavior of the cutting tool in a given cutting condition. The dynamic equation of motion in both $x$- and $y$-directions is given in Eq. 17, where $M$ is mass, $C$ is damping, and $K$ is stiffness matrices. Equation 17 can be solved numerically using Euler approximation as in Eqs. 18 to 20 to obtain the tool displacements in $x$- and $y$-directions. In these equations, $n$ is an integer number starting from one and $dt$ is the time-step.

$$\begin{bmatrix} M\ddot{x}(t) + C\dot{x}(t) + Kx(t) = F_X(t) \\ M\ddot{y}(t) + C\dot{y}(t) + Kx(t) = F_Y(t) \end{bmatrix} \tag{17}$$

$$\ddot{x}(t_n) = \frac{F_X(t_n) - c_x \dot{x}(t_n) - k_x x(t_n)}{m_x} \quad , \quad \ddot{y}(t_n)$$
$$= \frac{F_Y(t_n) - c_y \dot{y}(t_n) - k_y y(t_n)}{m_y} \tag{18}$$

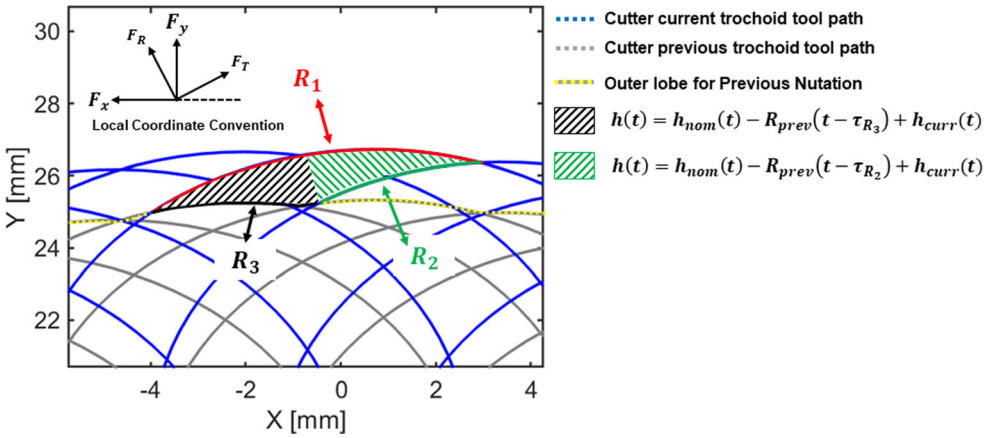


**Fig. 5** Three regions create a chip in trochoidal milling; instantaneous chip thickness is initially affected by $R_3$ when the tool enters the cut and then by $R_2$ while the tool exits the cut

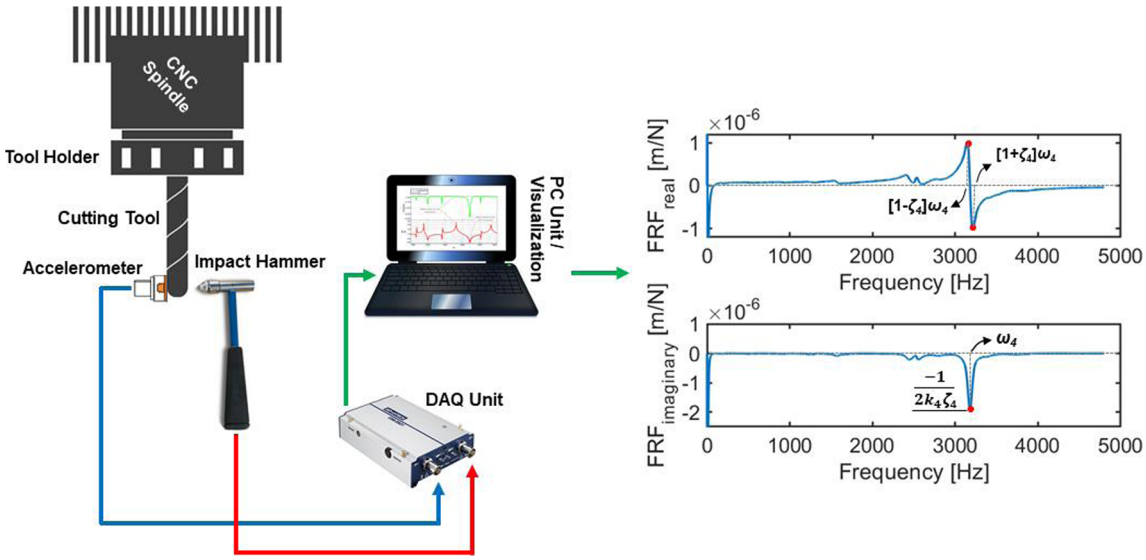


**Fig. 6** System dynamics characterization via modal testing unit

$$\dot{x}(t_n) = \dot{x}(t_{n-1}) + \ddot{x}(t_n)\mathrm{d}t \quad , \quad \dot{y}(t_n) = \dot{y}(t_{n-1}) + \ddot{y}(t_n)\mathrm{d}t \qquad (19)$$

$$x(t_n) = x(t_{n-1}) + \dot{x}(t_n)\mathrm{d}t \quad , \quad y(t_n) = y(t_{n-1}) + \dot{y}(t_n)\mathrm{d}t \qquad (20)$$

Considering the positive directions of Cartesian and polar coordinates shown in Fig. 3a, the magnitude of $F_X$ and $F_Y$ can be written as Eq. 21. Where $\vartheta$ and $\rho$ are switching functions and

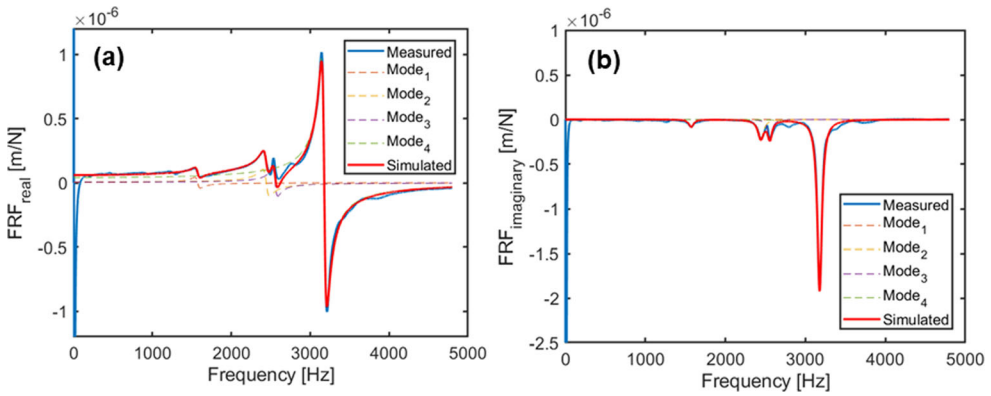


**Fig. 7** Comparison of simulated and measured FRF in *x*-direction, (**a**) real part and (**b**) imaginary part

$\tau_{R_2}$ and $\tau_{R_3}$ are the times that the tool is cutting through regions $R_2$ and $R_3$ in Fig. 5. Note that instantaneous chip thickness ($h$) follows the same formulation as in Eq. 5, except that the angle of rotation ($\theta$) is replaced with time ($t$). Considering Fig. 5, where three regions comprising a chip are shown with different colors, the vibration of the non-rigid tool is reflected on region $R_1$ where the cutter is currently located (the normal vibration magnitude is shown as $R_{\text{curr}}(t)$ in Eq. 21). The previously generated vibration on the surface can be decomposed into two regions. Region $R_3$ represents the vibrational contribution of previous nutation of the tool and region $R_2$ represents the vibrational contribution of the previous cutter pass. When the tool enters the cut, the instantaneous chip thickness is affected by current vibration of the tool and vibration on $R_3$ (i.e., previous nutation vibration). At some point in the cut, the cutter passes the region $R_3$ and enters the region $R_2$. After this point, the instantaneous chip thickness is affected by the current vibration of the tool as well as the vibration on $R_2$ (i.e., previous cutter vibration). As a result, a switching function is required for both regions $R_2$ and $R_3$ to isolate the effect of each region on chip thickness (see Eq. 22)

$$\begin{bmatrix} F_X(t) = -\sin(\theta)F_T - \cos(\theta)F_R = -\sin(\theta)K_t bh(t) - \cos(\theta)K_r bh(t) \\ F_Y(t) = -\cos(\theta)F_T + \sin(\theta)F_R = -\cos(\theta)K_t bh(t) + \sin(\theta)K_r bh(t) \\ \text{where} \quad h(t) = \left(h_{\text{nom}}(t) - R_{\text{prev}}(t - \vartheta(t)\tau_{R_2} - \rho(t)\tau_{R_3}) + R_{\text{curr}}(t)\right)g(t) \end{bmatrix} \tag{21}$$

$$\vartheta(t) = \begin{cases} 1 & t \in R_2 \\ 0 & t \notin R_2 \end{cases}, \quad \rho(t) = \begin{cases} 1 & t \in R_3 \\ 0 & t \notin R_3 \end{cases} \tag{22}$$

## 3 Experimental setup

### 3.1 Modal parameters identification

All the tests were conducted on a 5-axis OKUMA MU-5000V CNC machine with Sandvik R390-016EH16-11L double-flute tool holder and Sandvik Coromill R390-11T308M-PM-1030 carbide inserts with tool radius ($R_d$) of 7.94 mm. Modal testing was carried out with an impact hammer with a medium-impact tip for excitation of the "tool-spindle" dynamic system in order to identify modal parameters. The vibration response of the system was captured through an accelerometer (sensitivity 5 mV/g, resolution 0.03 m/s$^2$ rms) attached to the modal hammer (sensitivity 1.1 mV/N, resolution ± 4448 N pk). Both excitation force and vibration response signals were later converted in signal analyzer from time domain into frequency domain to generate direct FRF in $x$- and $y$-directions (see Fig. 6).

To be able to extract the modal mass, stiffness, and damping from FRF measurements, a peak picking method was utilized (see Appendix A for details). As shown in Fig. 6, four mode shapes are visually detectable in $x$-direction (and also $y$-direction, which is not shown here) up to the frequency range of 5 kHz. In this figure, the parameter $\zeta_i$ is the damping ratio, $k_i$ is the modal stiffness, $\omega_i$ is the natural frequency, and $i \in \{1,2,3,4\}$. The simulated FRF is compared with the measured FRF in Fig. 7, where a good degree of agreement can be observed. The error was quantified between simulated and measured values of real FRF in local extrema points, and maximum error of 30% was observed which occurs around the 3rd natural frequency. The same process was repeated to identify modal parameters in $y$-direction. In Table 1, the identified modal parameters are summarized.

All the testing samples were cut from a block of IN718 nickel-based superalloy to ensure consistency in the microstructure and mechanical behavior of samples. The force signal was captured with sampling frequency of 5 kHz using a Kistler 9257B piezoelectric dynamometer. The Design of Experiments (DoE) table with trochoidal tool path parameters ($\dot{\theta}$, $\dot{\phi}$, and $\nu$) and

**Table 1** Identified modal parameters in both $x$- and $y$- directions

| Modal properties in $x$-direction | | | | |
|---|---|---|---|---|
| Mode [#] | $\omega_{nx}$ [Hz] | $m_x$ [kg] | $c_x$ [N.m/s] | $k_x$ [N/m] |
| 1 | 1573 | 106 | $1.2 \times 10^3$ | $2.6 \times 10^8$ |
| 2 | 2443 | 23 | 308 | $1.4 \times 10^8$ |
| 3 | 2556 | 28 | 295 | $1.8 \times 10^8$ |
| 4 | 3178 | 2.4 | 26 | $2.4 \times 10^7$ |
| Modal properties in $y$-direction | | | | |
| Mode [#] | $\omega_{ny}$ [Hz] | $m_y$ [kg] | $c_y$ [N.m/s] | $k_y$ [N/m] |
| 1 | 1481 | 148 | $1.9 \times 10^3$ | $3.2 \times 10^8$ |
| 2 | 2411 | 32 | 347 | $1.9 \times 10^8$ |
| 3 | 2562 | 18 | 296 | $1.2 \times 10^8$ |
| 4 | 3173 | 2.5 | 22 | $2.46 \times 10^7$ |

**Table 2** DoE table for trochoidal milling with double-flute tool; tool rotation radius ($R_{cp}$) was selected as 10.06 mm in all the experiments

| | Trochoidal tool path parameters | | | | CNC machine equivalent parameters |
|---|---|---|---|---|---|
| Number [#] | Step-over feedrate $\nu$ [mm/s] | Nutation rate $\dot{\phi}$ [rad/s] | Rotational rate $\dot{\theta}$ [RPM] | Axial depth of cut $b$[mm] | Feed per tooth $f$ [mm/tooth] |
| T1 | 0.025 | 0.3 | 400 | 0.50 | 0.357 |
| T2 | 0.025 | 0.5 | 1200 | 1.00 | 0.198 |
| T3 | 0.025 | 0.7 | 600 | 0.75 | 0.556 |

**Table 3** Identified cutting pressure coefficients for each experiment

| Number [#] | Tangential cutting pressure coeff. $K_T$ [N/mm$^2$] | Radial cutting pressure coeff. $K_R$ [N/mm$^2$] |
|---|---|---|
| T1 | 4891 | 3044 |
| T2 | 5252 | 4516 |
| T3 | 5097 | 2690 |

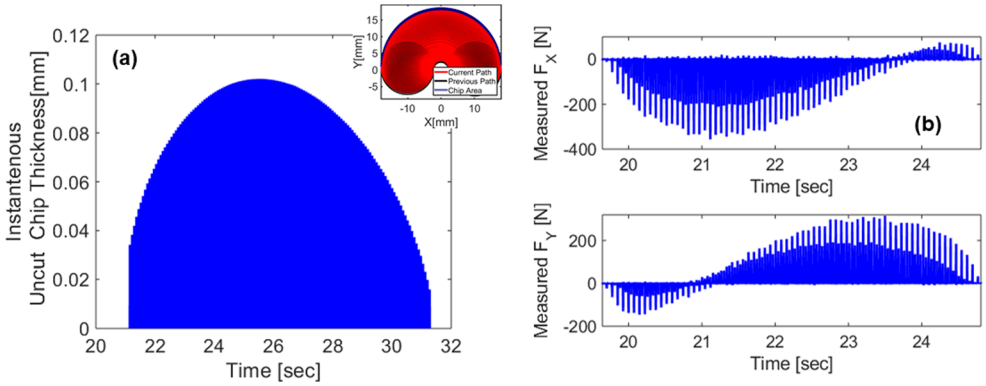


**Fig. 8** Cutting pressure coefficients are calculated using the **a** simulated uncut chip thickness and **b** measured forces—results are given for experiment T1

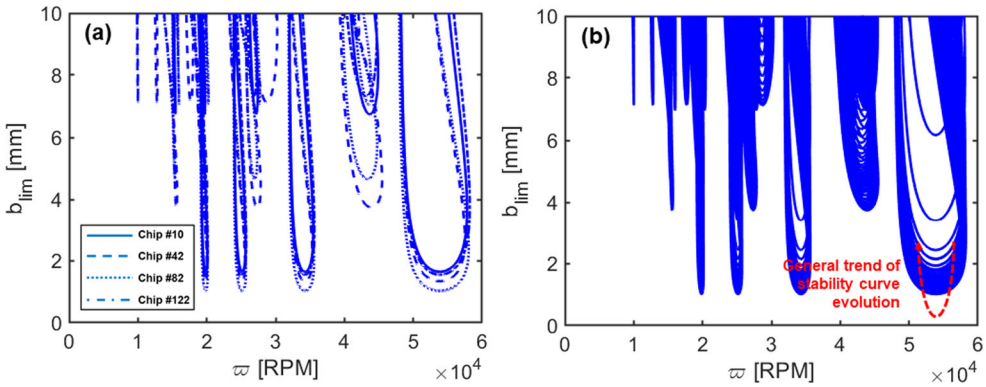


**Fig. 9** Dynamic stability curve, evolution per chip in experiment T1, **a** stability curves for the beginning, middle, and end of a full nutation; and **b** complete stability curves for a full nutation (total of 136 chips)

corresponding machine parameters (RPM, feed per tooth) are given in Table 2 (refer to [17] on the process of converting trochoidal tool path parameters to machine parameters). High strength and poor thermal conductivity of IN718 superalloy expose the cutting tool to extremely high pressure and temperature which could potentially reduce the tool lifetime or make it prone to premature catastrophic failure. Therefore, there are practical challenges in increasing spindle speed and depth of cut in cutting IN718 and many trial tests were carried out to identify the feasible regions of machining in which the cutting tool lasts for a slot length of 80 mm. To avoid tool wear effects on the simulation results, it was decided to stop the experiments intermittently and to measure the tool wear in order to ensure that flank wear does not exceed 40 μm.

The tangential and radial cutting pressure coefficients ($K_T$ and $K_R$) were calculated for each test after converting the measured forces ($F_X$ and $F_Y$) into polar coordinate and dividing $F_T$ and $F_R$ by calculated chip thickness. The calculated cutting pressure coefficients for all the experiments are given in Table 3. The calculated chip thickness and measured cutting forces for the experiment T1 are given in Fig. 8 to provide an example of chip thickness and force variation over time.

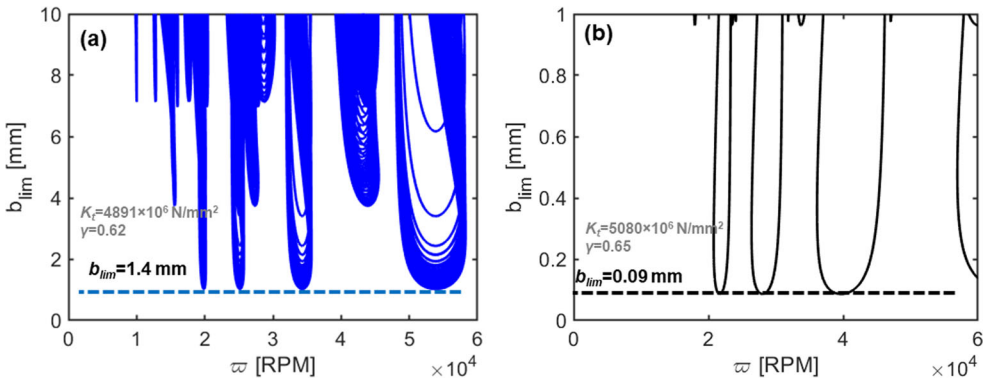


**Fig. 10** Chatter stability limit for **a** trochoidal test T1 and **b** slot milling test

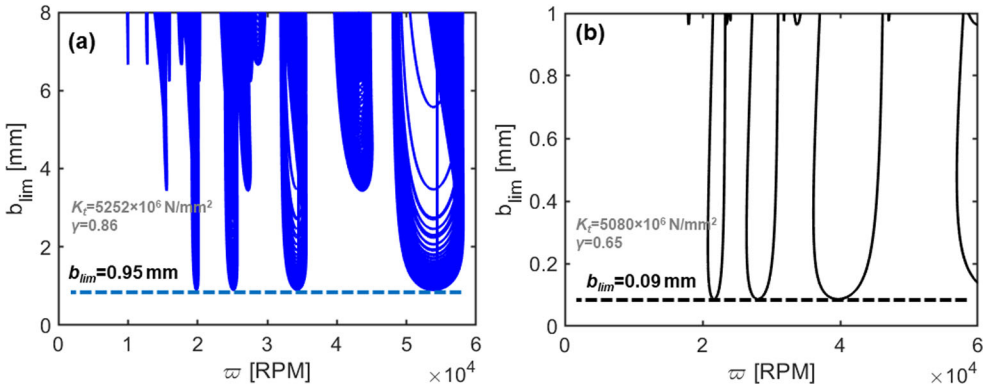


**Fig. 11** Chatter stability limit for **a** trochoidal test T2 and **b** slot milling test

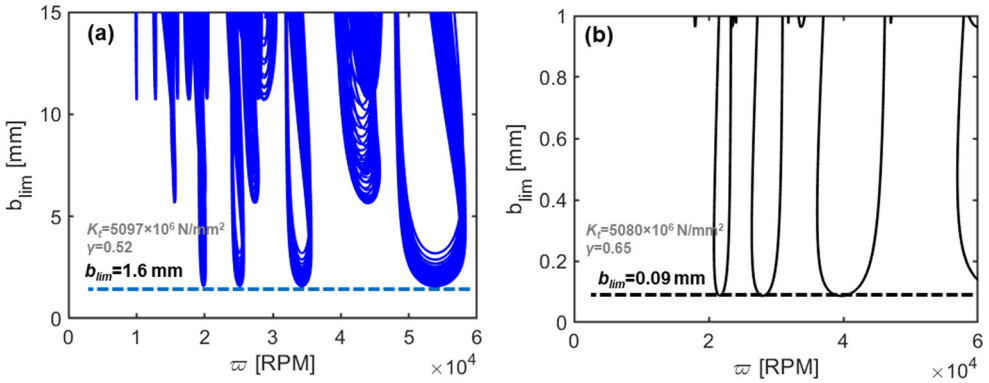


**Fig. 12** Chatter stability limit for **a** trochoidal test T3 and **b** slot milling test

## 4 Results and discussion

### 4.1 Chatter stability in Trochoidal milling

Using Eqs. 14 to 16, chatter stability curves can be created for the trochoidal tool path. As mentioned in Section 2.2, due to the change in shape and orientation (i.e., change in tool entering and exiting angles) of the chips in a full nutation of the tool, the matrix $A$ in Eq. 7 needs to be updated for each individual chip. This leads to generation of a family of unique chatter curves per chip that evolve over time. To better demonstrate this, the stability curve for only four chips at the beginning ($[\theta_{enter},\ \theta_{exit}]_{Chip\#10} = [31^o,\ 12^o]$), middle ($[\theta_{enter},\ \theta_{exit}]_{Chip\#42} = [81^o,\ 52^o]$ and $[\theta_{enter},\ \theta_{exit}]_{Chip\#82} = [132^o,\ 104^o]$), and near the end ($[\theta_{enter},\ \theta_{exit}]_{Chip\#122} = [172^o,\ 155^o]$) of a full nutation is shown in Fig. 9a. As in this figure, each chip has its own stability criteria and critical depth of cut limit evolves with the nutation of the tool. It is observed that at the beginning and the end of the cut where chip thickness is the least, the depth of cut limit ($b_{lim}$) has the highest value, whereas in the middle of the cut where the chip thickness reaches its peak, the $b_{lim}$ reaches its minimum.

The tangential cutting pressure coefficients directly affects the limit of the axial depth of cut (see Eq. 14); therefore it is necessary to reevaluate the stability curves based on cutting pressure coefficients for all three experiments of Table 2. This is shown in Figs. 10a, 11a, and 12a. It is also worth comparing

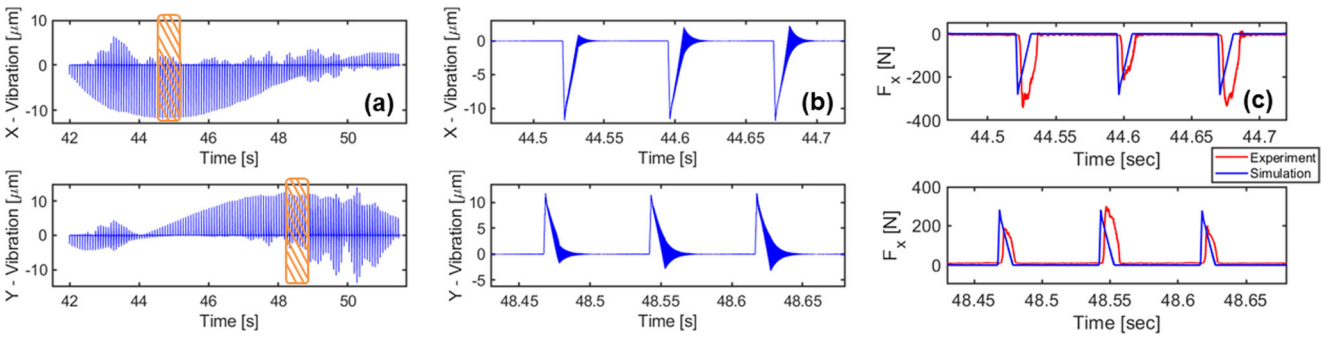


**Fig. 13** Simulated displacement and force in test T1, **a** tool displacement in full nutation, **b** detailed vibrational response of the hatched area, and **c** comparison of simulated and experimental force of the hatched area

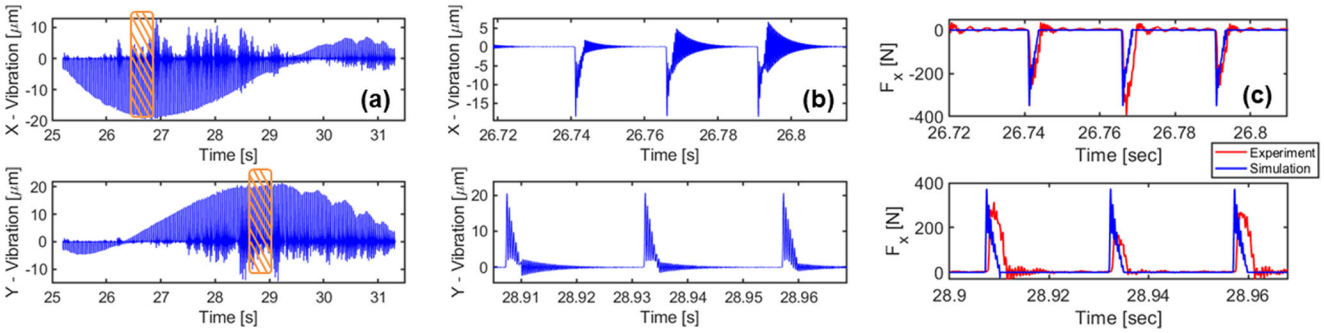


**Fig. 14** Simulated displacement and force in test T2, **a** tool displacement in full nutation, **b** detailed vibrational response of the hatched area, and **c** comparison of simulated and experimental force of the hatched area

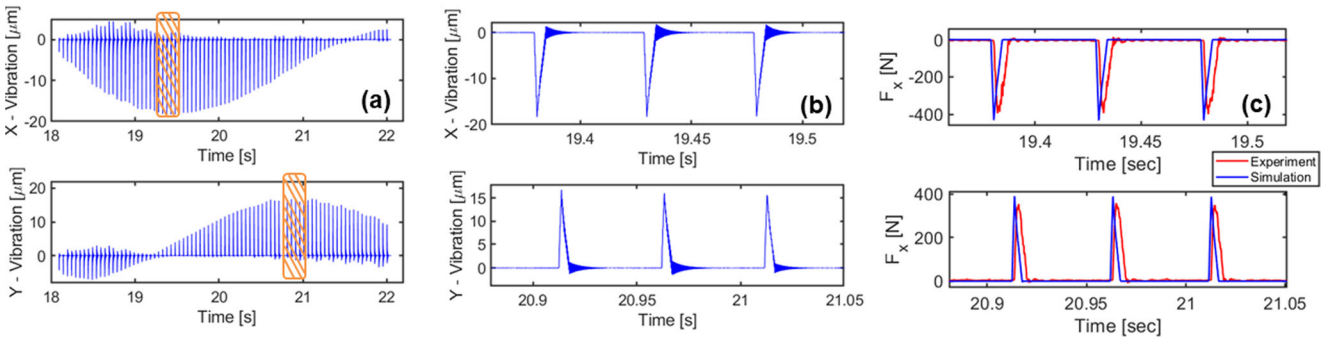


**Fig. 15** Simulated displacement and force in test T3, **a** tool displacement in full nutation, **b** detailed vibrational response of the hatched area, and **c** comparison of simulated and experimental force of the hatched area

the stability curves and limit of axial depth of cut between trochoidal and conventional end-milling scenarios. Assuming $K_T$ = 5080 MPa and $\gamma = 0.65$ as the average of $K_T$ and $\gamma$ values in Table 3, the slot milling stability diagram can be generated. As shown in Figs. 10b, 11b, and 12b, the depth of cut limit for slot milling is significantly smaller (at least ten times) than trochoidal milling tests which can be attributed to the partial engagement of the cutter in trochoidal milling. As discussed in [17], low radial engagement in trochoidal milling provides the opportunity to the user to greatly increase the depth of cut while maintaining the stability of the machining process. The higher depth of cut allows for higher volume of material removed which leads to increased productivity in comparison to conventional end-milling strategy, a significantly critical factor in selecting proper tool path from industrial standpoint.

## 4.2 Time domain simulation of tool vibration in trochoidal milling

Considering the second order dynamic equation of motion given in Eq. 17 and identified modal parameters of tool-spindle-machine system given in Table 1, a time domain simulation can be conducted for each experiment. For simplicity and decreasing run-time in the simulation, it is assumed that the tool vibrates as a single-degree of freedom system with dynamic characteristics of the mode with lowest stiffness (mode 4 in Table 1). In addition, the boundary conditions of the tool (i.e., initial displacement and velocity in both $x$- and $y$-coordinates) are set equal to zero to initiate the numerical simulation. As explained in Section 2.3 and shown in Fig. 5, initially when the cutter enters the chip, the instantaneous chip thickness is affected by vibrational contribution of previous nutation (term $R_{\text{prev}}(t-\rho(t)\tau_{R_3})$ in Eq. 21). At some point in the middle of the cut, this vibrational contribution shifts from previous nutation to previous cutter (term $R_{\text{prev}}(t-\vartheta(t)\tau_{R_2})$ in Eq. 21). Therefore, to be able to truly capture the tool's displacement effect on chip thickness, the simulation should be executed for two consecutive nutations. In the first nutation ($0^o < \phi < 180^o$), no vibrational effect due to $R_3$ (see Fig. 5) is assumed and $R_{\text{prev}}(t-\rho(t)\tau_{R_3}$ in Eq. 21 is set equal to zero. Therefore, the instantaneous chip thickness is assumed to be only affected by the cutter's current vibration and the previous cutter vibration (i.e. vibration created in $R_2$). The tool displacement results are saved to be used for a second nutation (where a portion of $R_1$ defines region $R_3$ of second nutation). This way, the time domain simulation produces tool displacement results considering both the vibrational contribution of the previous nutation and previous cutter pass.

**Table 4** Selected modal properties in $x$- and $y$-direction

| $x$-direction | | |
|---|---|---|
| $m_x$ [kg] | $c_x$ [N.m/s] | $k_x$ [N/m] |
| 10.6 | 34.5 | $2.4 \times 10^5$ |
| $y$-direction | | |
| $m_y$ [kg] | $c_y$ [N.m/s] | $k_y$ [N/m] |
| 10.9 | 29.1 | $2.4 \times 10^4$ |

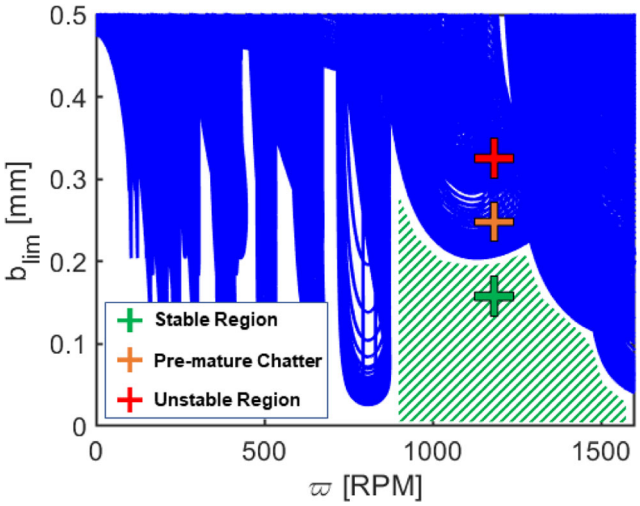


**Fig. 16** Stability diagram for a spindle system with a given modal parameters in Table 4, three depths of cut in constant rotation rate of 1100RPM is chosen for time domain simulation

The tool vibration and simulated force results are given Figs. 13, 14, and 15 for all three experiments. As can be inferred from chatter stability curves discussed in Section 4.1, the tool remains in stable cutting region in all the experiments. This can also be seen in Figs. 13a, 14a, and 15a, where the tool vibration does not exceed 20 μm in both *x*- and *y*-directions. The free vibration of the tool with its natural frequency is also observable at the point where the cutter exits the chip in Figs. 13b, 14b, and 15b. Moreover, the simulated dynamic force is compared with the measured force in the region where the maximum force occurs and is given in Figs. 13c, 14c, and 15c. Note that the small displacement of the tool particularly in tests T1 and T3 does not affect the cutting force significantly. However, a large displacement was observed in test T2 (~ 20 μm) with its magnitude is comparable to the maximum chip thickness generated in this test (~ 45 μm). As a result, significant jitter in simulated cutting force is observable in Fig. 14c.

To be able to simulate the dynamic force and displacement of the tool and transition from stable to unstable (chatter) regions, two criteria are required. First, in a given spindle rotation, increasing the axial depth of cut and second in a given depth of cut, increasing the spindle rotation will initiate chatter. From a practical point of view, this is not feasible in cutting IN718 nickel-based superalloys. As explained in Section 1, the extremely high strength and low thermal conductivity of this alloy restrict the user's choice of cutting parameters to a small region. The authors conducted experiments in spindle speeds beyond 2000 RPM but catastrophic failure of the tool was commonly observed during the first nutation. Therefore, the range between 600 and 1500 RPM was selected for the DoE which also agrees with the tool manufacturer heuristic cutting criteria suggestions in trochoidal milling of nickel-based superalloys. It should be noted that in these selected range of spindle speeds, the limiting depth of cut to initiate chatter is above 8 mm, which makes

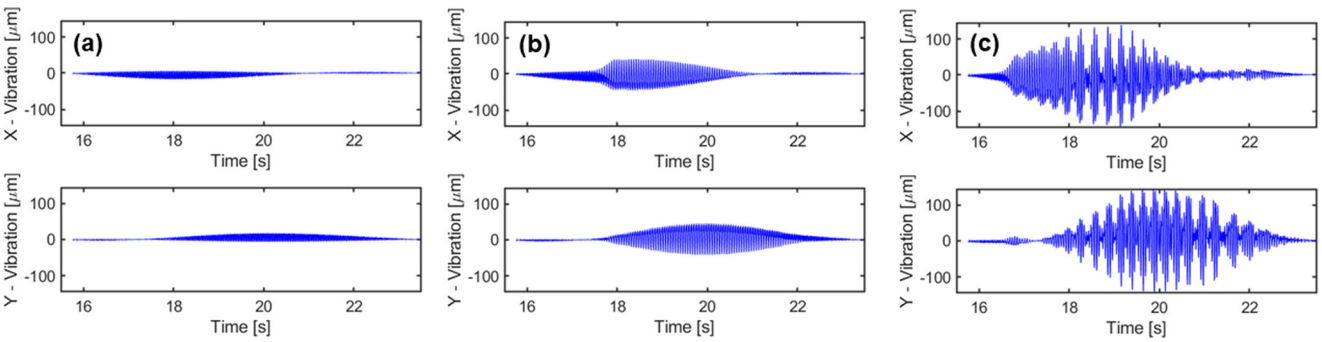


**Fig. 17** Tool displacement in a given spindle rotation and variable depth of cut, **a** stable cut with depth of cut of 0.15 mm, **b** premature chatter with depth of cut of 0.22 mm, and **c** unstable cut with depth of cut of 0.32 mm

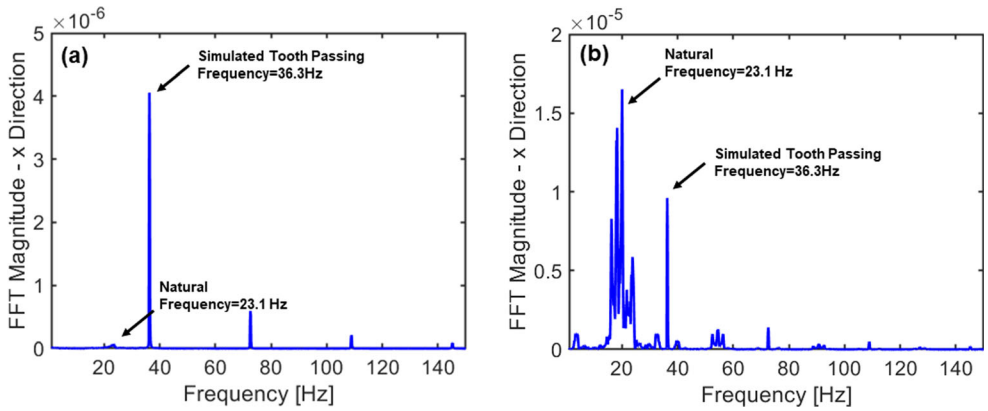


**Fig. 18** FFT analysis on the simulated tool displacement, **a** stable cutting with $b = 0.15$ mm and, **b** unstable cutting with $b = 0.32$ mm

**Table 5** Comparison of theoretical and simulated natural frequency and tooth passing frequency

| | From theory | From simulation (FFT analysis) |
|---|---|---|
| Natural frequency [Hz] | 24 | 23.1 |
| Tooth passing frequency [Hz] | 36.6 | 36.3 |

testing stability of machining IN718 nearly impossible due to the combination of high material strength and high chip load in comparison to limited strength of the cutting tool. Therefore, it was decided to simulate the machine response in the stable, transition, and unstable zones in a more compliant machine defined by the modal parameters given in Table 4. First, the chatter stability diagram in trochoidal milling for a test with cutting parameters ($\dot{\phi}$ = 0.4 rad/s, $\dot{\theta}$ = 1100 RPM, and $v_{feed}$ = 0.05 mm/s) is created and is shown in Fig. 16. The green zone in Fig. 16 is a region where no chatter should be observed. By increasing the depth of cut, the tool enters a transitional zone between stable and unstable cut. In other words, the tool undergoes chatter in only a portion of chips and in the rest of the other chips, the tool stays in stable region (premature chatter). By increasing the depth of cut to 0.32 mm, the tool remains in unstable region for more than 80% of the chips, and therefore chatter occurs throughout the full nutation of the tool. The displacement of the tool is given in Fig. 17 for all three depths of cut. Note that the *y*-axis in Fig. 17 is chosen based on maximum displacement in order to enable the reader to compare the overall tool displacement in stable (maximum displacement of 16 μm), premature chatter (maximum displacement of 40 μm), and chatter regions (maximum displacement of 140 μm, where tool disengagement was observed).

The time domain simulation in stable and unstable cuts must contain information of the tooth passing and natural frequencies. Therefore, a fast Fourier transform (FFT) was performed on the displacement signal (in *x*-direction only); the results are shown in Fig. 18. As can be seen in Fig. 18a, in the stable cutting region ($b$ = 0.15 mm), the energy of the natural frequency is significantly lower than the energy of the tooth passing frequency. However, in Fig. 18b where the tool vibrates in the chatter region, a significant spike in the energy of the signal around the natural frequency is observed. The simulated natural frequency and tooth passing frequency based on FFT analysis is compared with the theoretical natural frequency ($=\sqrt{k_x/m_x}$ from Table 4) and tooth passing frequency ($= 1100 \times \frac{2}{60}$ Hz) in Table 5.

## 5 Summary, conclusions, and future directions

The objective of this work was to investigate the effect of the trochoidal tool path on stability in milling IN718 nickel-based superalloy. In the previous work of the authors, a chip thickness model based on a numerical intersection-finding method was established for a rigid tool-spindle system. In this work, the assumption of tool-spindle rigidity was removed, and the non-rigid dynamic system was analyzed and proper formulation extracted to establish chatter stability curves for true trochoidal milling. Furthermore, a time domain simulation was performed to study the instantaneous chip thickness and tool displacement. The summary of the work is given below:

- The fast Fourier approach for establishing milling stability proposed in [23] was reformulated to account for variable chip thickness and chip geometry in the trochoidal tool path. It was shown that since the tool enters and exits each chip with different angles, a unique stability curve must be attributed to each individual chip, where the critical depth of cut ($b_{lim}$) varies based on thickness and orientation. In other words, it is possible in trochoidal milling to select a depth of cut higher than the smallest critical depth of cut ($b_{lim\_minimum}$) and still avoid chatter since chatter is initiated in only a portion of the chips with their individual $b_{lim}$ bigger than selected depth of cut, while the rest of the chips do not undergo any chatter. As a result, full vibrational instability remains premature and chatter can be avoided.
- Modal testing was conducted to extract the modal parameters of the spindle-tool system and local stability of the tests was studied in a time domain simulation. It was shown that the results of time domain simulation can capture stability or instability of the cut. FFT analysis was also performed on the simulated tool displacement with an expectation to detect a natural frequency with high spectral energy in the unstable cut.

Combining the results of this work on dynamic stability analysis of trochoidal milling and previous work of authors on static chip thickness modeling provides a comprehensive framework to the user to better understand the process and be able to fine-tune it before running extensive trial testing. This is of significant importance when working with nickel-based superalloys, where material and tooling cost are major challenges for industrial users. While this work is establishing a groundwork of dynamic stability analysis in trochoidal milling, there is still room for improvement. First, the Fourier approach used for formulating the stability curves is mostly accurate for a milling operation with high radial immersion. However, trochoidal milling is considered as a low radial immersion process and therefore the methods of stability analysis based on low radial immersion [24, 25] need to be investigated and benchmarked with current methods; this is a future direction of this work. Also, tool wear is a critical factor in cutting superalloys. To avoid wear effects on cutting pressure coefficients and stability prediction, the operation was stopped before tool flank wear reaches a minimum limit of just 40 μm. Therefore, wear effects were neglected. Studying the effect of wear on dynamic stability of the process is the second direction considered for future work. Furthermore, extending the application of trochoidal milling to non-metals, such as cutting plastics for automotive applications

with growing market usage of plastics and composites [26], is another direction that is worthy of investigation.

**Funding information** The authors would like to thank the National Science Foundation for supporting this work under Grant No. 1760809.

## Compliance with ethical standards

**Disclaimer** Any opinions, findings, and conclusions or recommendations expressed in this material are those of the authors and do not necessarily reflect the views of the National Science Foundation.

## Appendix 1

Considering a single degree of freedom dynamic system, the ratio of displacement response with respect of input force can be written as Eq. A1. Where $X$ is displacement and $F$ is input force. By taking the derivative of imaginary part of $X/F$ with respect to $\omega/\omega_n$, it can be shown that when $\omega/\omega_n$ is equal to 1, the imaginary part reaches its peak value of $-1/2k\zeta$. In other words, at natural frequency ($\omega=\omega_n$), the imaginary part of FRF has its peak value equal to $-1/2k\zeta$. The same procedure can be written for the real FRF where local extrema can be found as $\omega/\omega_n=(1\pm2\zeta)^{1/2}$. Considering small values of $\zeta$, when $\zeta^2$ can be neglected, $\omega/\omega_n$ can be approximated as $1\pm\zeta$.

Therefore, the peak picking method can be summarized as follows: the natural frequency of a system can be found where the imaginary part of FRF reaches its peak. By having access to natural frequency of the system, and reading the $\omega/\omega_n$ values from real part of FRF at a local minima or local maxima, the damping ratio $\zeta$ can be found. Having access to $\zeta$ and the magnitude of peak value of imaginary FRF, the modal stiffness $k$ can be found. With the combination of modal stiffness $k$, damping ratio $\zeta$, and natural frequency $\omega_n$, the rest of modal parameters (i.e., modal mass $m$ and modal damping $c$) will be calculated.

$$\begin{aligned}\mathrm{Re}\left(\frac{X}{F}\right)&=\frac{1}{k}\left(\frac{1-(\omega/\omega_n)^2}{\left(1-(\omega/\omega_n)^2\right)^2+(2\zeta\omega/\omega_n)^2}\right)\\ \mathrm{Im}\left(\frac{X}{F}\right)&=\frac{1}{k}\left(\frac{-2\zeta\omega/\omega_n}{\left(1-(\omega/\omega_n)^2\right)^2+(2\zeta\omega/\omega_n)^2}\right)\end{aligned}\tag{A1}$$

Due to the principle of superposition for linear systems, if multiple degrees of freedom exist, then the direct FRF is the summation of contribution of each degree of freedom where it can be calculated as Eq. A2.

$$\frac{X}{F}=\sum_{i=1}^{m}\frac{1}{k_m}\left(\frac{\left(1-(\omega_m/\omega_{nm})^2\right)-i(2\zeta_m\omega_m/\omega_{nm})}{\left(1-(\omega_m/\omega_{nm})^2\right)^2+(2\zeta_m\omega_m/\omega_{nm})^2}\right)\tag{A2}$$

## Appendix 2

Assuming the positive direction shown in Fig. 3, the normal vibration in radial direction can be written as in Eq. A1, where $r$ is displacement in radial direction and $x$ and $y$ are tool displacements in Cartesian coordinate system. By substituting Eq. B1 in Eq. 5 and neglecting the constant term ($h_{\mathrm{nom}}^{\{N\}}$), Eq. B2 can be written.

$$r=-x\cos(\theta)+y\sin(\theta)\tag{B1}$$

$$\begin{aligned}h^{\{N\}}(\theta)&=\left(x_{\mathrm{prev}}\cos(\theta)-y_{\mathrm{prev}}\sin(\theta)-x_{\mathrm{curr}}\cos(\theta)+y_{\mathrm{curr}}\sin(\theta)\right)g(\theta)\\&=\left(-\cos(\theta)\left(x_{\mathrm{curr}}-x_{\mathrm{prev}}\right)+\sin(\theta)\left(y_{\mathrm{curr}}-y_{\mathrm{prev}}\right)\right)g(\theta)\\&=\left(-\Delta x\cos(\theta)+\Delta y\sin(\theta)\right)g(\theta)\end{aligned}\tag{B2}$$

By plugging Eq. B2 into Eq. 3, the dynamic part of radial and tangential force can be found. Using the rotational matrix $R$ given in Eq. 4, and after some trigonometric manipulation the dynamic forces in $x$- and $y$-directions are derived as Eqs. B3 and B4.

$$\begin{aligned}F_X&=-F_T\sin(\theta)-F_R\cos(\theta)\\&=-K_Tb\left(\left(-\Delta x\cos(\theta)+\Delta y\sin(\theta)\right)g(\theta)\right)\sin(\theta)-\gamma K_Tb\left(\left(-\Delta x\cos(\theta)+\Delta y\sin(\theta)\right)g(\theta)\right)\cos(\theta)\\&=\frac{1}{2}K_Tb\left(\sin(2\theta)+\gamma\left(1+\cos(2\theta)\right)\right)g(\theta)\Delta x+\frac{1}{2}K_Tb\left(1-\cos(2\theta)+\gamma\sin(2\theta)\right)g(\theta)\Delta y\end{aligned}\tag{B3}$$

$$\begin{aligned}F_Y&=-F_T\cos(\theta)+F_R\sin(\theta)\\&=-K_Tb\left(\left(-\Delta x\cos(\theta)+\Delta y\sin(\theta)\right)g(\theta)\right)\cos(\theta)+\gamma K_Tb\left(\left(-\Delta x\cos(\theta)+\Delta y\sin(\theta)\right)g(\theta)\right)\sin(\theta)\\&=\frac{1}{2}K_Tb\left(1+\cos(2\theta)-\gamma\sin(2\theta)\right)g(\theta)\Delta x+\frac{1}{2}K_Tb\left(\sin(2\theta)-\gamma\left(1-\cos(2\theta)\right)\right)g(\theta)\Delta y\end{aligned}\tag{B4}$$

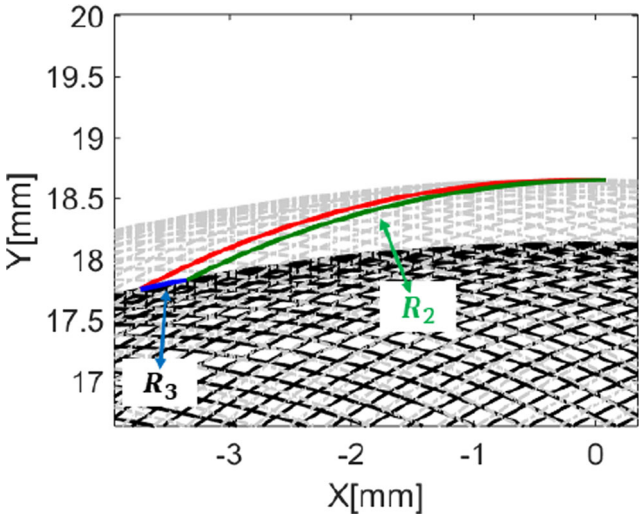


**Fig 19** Chip geometry for Test T1; the R3 region (effect of previous nutation) is significantly smaller than R2

Combing Eqs. B3 and B4 into a matrix format, Eq. 6 can be found. Note that in this derivation, it was assumed the portion of the chip geometry affected by $R_3$ region (previous nutation) is significantly smaller than the other portion of the chip created by $R_2$ region (previous cutter). This assumption is valid since in the DoE table, the rotational rate is chosen much higher than nutation rate and therefore $R_3$ region will be significantly smaller than $R_2$. This is shown in Fig. 19.

## Appendix 3

Considering Eq. 10 for vibration of current cutter and vibration of the previous cutter, Eq. C1 can be written.

$$\begin{bmatrix}\Delta X\\ \Delta Y\end{bmatrix} = \begin{bmatrix}X_{\text{curr}}\\ Y_{\text{curr}}\end{bmatrix} - \begin{bmatrix}X_{\text{prev}}\\ Y_{\text{prev}}\end{bmatrix} = \begin{bmatrix}FRF_{XX} & 0\\ 0 & FRF_{YY}\end{bmatrix}\begin{bmatrix}F_X\\ F_Y\end{bmatrix} e^{i\omega_c t}\left(1-e^{-i\omega_c \tau}\right) \quad \text{(C1)}$$

By writing the Eq. 6 in frequency domain (Eq. C2), and substituting Eq. B1 in C2, Eq. C3 can be found.

$$\begin{bmatrix}F_X\\ F_Y\end{bmatrix} e^{i\omega_c t} = \frac{1}{2} bK_T[A]\begin{bmatrix}\Delta X\\ \Delta Y\end{bmatrix} \quad \text{(C2)}$$

$$\begin{bmatrix}F_X\\ F_Y\end{bmatrix} e^{i\omega_c t} = \frac{1}{2} bK_T[A]\begin{bmatrix}FRF_{XX} & 0\\ 0 & FRF_{YY}\end{bmatrix}\begin{bmatrix}F_X\\ F_Y\end{bmatrix} e^{i\omega_c t}\left(1-e^{-i\omega_c \tau}\right) \quad \text{(C3)}$$

Re-arranging Eq. C3 gives Eq. C4. In order for Eq. C4 to have a non-trivial answer, its determinant given in Eq. C5 should be zero. This is the characteristic equation of chatter.

$$\begin{bmatrix}F_X\\ F_Y\end{bmatrix} e^{i\omega_c t}\left(I - \frac{1}{2} bK_T[A]\begin{bmatrix}FRF_{XX} & 0\\ 0 & FRF_{YY}\end{bmatrix}\left(1-e^{-i\omega_c \tau}\right)\right) = 0 \quad \text{(C4)}$$

$$\det\left(I - \frac{1}{2} bK_T[A]\begin{bmatrix}FRF_{XX} & 0\\ 0 & FRF_{YY}\end{bmatrix}\left(1-e^{-i\omega_c \tau}\right)\right) = 0 \quad \text{(C5)}$$



## References


1. Long H, Mao S, Liu Y, Zhang Z, Han X (2018) Microstructural and compositional design of Ni-based single crystalline superalloys — a review. J Alloys Compd 743:203–220. https://doi.org/10.1016/J.JALLCOM.2018.01.224
2. Thakur A, Gangopadhyay S (2016) State-of-the-art in surface integrity in machining of nickel-based super alloys. Int J Mach Tools Manuf 100:25–54. https://doi.org/10.1016/j.ijmachtools.2015.10.001
3. Zhu D, Zhang X, Ding H (2013) Tool wear characteristics in machining of nickel-based superalloys. Int J Mach Tools Manuf 64:60–77
4. Corne R, Nath C, El Mansori M (2017) Study of spindle power data with neural network for predicting real-time tool wear/breakage during inconel drilling. J Manuf Syst 43:287–295. https://doi.org/10.1016/J.JMSY.2017.01.004
5. Akhavan Niaki F, Feng L, Ulutan D, Mears L (2016) A wavelet-based data-driven modelling for tool wear assessment of difficult to machine materials. Int J Mechatronics Manuf Syst 9:97–121
6. Kong D, Chen Y, Li N, Tan S (2017) Tool wear monitoring based on kernel principal component analysis and v-support vector regression. Int J Adv Manuf Technol 89:175–190. https://doi.org/10.1007/s00170-016-9070-x
7. Wang J, Xie J, Zhao R, Zhang L, Duan L (2017) Multisensory fusion based virtual tool wear sensing for ubiquitous manufacturing. Robot Comput Integr Manuf 45:47–58. https://doi.org/10.1016/J.RCIM.2016.05.010
8. Akhavan Niaki F, Michel M, Mears L (2016) State of health monitoring in machining: extended Kalman filter for tool wear assessment in turning of IN718 hard-to-machine alloy. SI NAMRC 24(Part 2):361–369
9. Akhavan Niaki F, Ulutan D, Mears L (2015) Stochastic tool wear assessment in milling difficult to machine alloys. Int J Mechatronics Manuf Syst 8:134–159
10. Zhang J, Starly B, Cai Y, Cohen PH, Lee YS (2017) Particle learning in online tool wear diagnosis and prognosis. J Manuf Process 28:457–463. https://doi.org/10.1016/J.JMAPRO.2017.04.012
11. Yu J, Liang S, Tang D, Liu H (2017) A weighted hidden Markov model approach for continuous-state tool wear monitoring and tool life prediction. Int J Adv Manuf Technol 91:201–211. https://doi.org/10.1007/s00170-016-9711-0
12. Wu D, Jennings C, Terpenny J, Gao RX, Kumara S (2017) A comparative study on machine learning algorithms for smart manufacturing: tool wear prediction using random forests. J Manuf Sci Eng 139:071018. https://doi.org/10.1115/1.4036350
13. Pleta A, Ulutan D, Mears L (2014) Investigation of trochoidal milling in nickel-based superalloy inconel 738 and comparison with end milling. In: ASME 2014 International Manufacturing Science and Engineering Conference collocated with the JSME 2014

International Conference on Materials and Processing and the 42nd North American Manufacturing Research Conference. American Society of Mechanical Engineers, p V002T02A058-V002T02A058
14. Kardes N, Altintas Y (2007) Mechanics and dynamics of the circular milling process. J Manuf Sci Eng 129:21. https://doi.org/10.1115/1.2345391
15. Otkur M, Lazoglu I (2007) Trochoidal milling. Int J Mach Tools Manuf 47:1324–1332
16. Deng Q, Mo R, Chen ZC, Chang Z (2018) A new approach to generating trochoidal tool paths for effective corner machining. Int J Adv Manuf Technol 95:3001–3012. https://doi.org/10.1007/s00170-017-1353-3
17. Akhavan Niaki F, Pleta A, Mears L (2018) Trochoidal milling: investigation of a new approach on uncut chip thickness modeling and cutting force simulation in an alternative path planning strategy. Int J Adv Manuf Technol 97:641–656. https://doi.org/10.1007/s00170-018-1967-0
18. Yan R, Li H, Peng F, Tang X, Xu J, Zeng H (2017) Stability prediction and step optimization of Trochoidal milling. J Manuf Sci Eng 139:091006. https://doi.org/10.1115/1.4036784
19. Rauch M, Duc E, Hascoet J-Y (2009) Improving trochoidal tool paths generation and implementation using process constraints modelling. Int J Mach Tools Manuf 49:375–383. https://doi.org/10.1016/J.IJMACHTOOLS.2008.12.006
20. Toh CK (2003) Tool life and tool wear during high-speed rough milling using alternative cutter path strategies. Proc Inst Mech Eng Part B J Eng Manuf 217:1295–1304
21. Shixiong W, Wei M, Bin L, Chengyong W (2016) Trochoidal machining for the high-speed milling of pockets. J Mater Process Technol 233:29–43. https://doi.org/10.1016/J.JMATPROTEC.2016.01.033
22. Uhlmann E, Fürstmann P, Rosenau B, et al (2013) The potential of reducing the energy consumption for machining TiAl6V4 by using innovative metal cutting processes. In: 11th global conference on sustainable manufacturing. Berlin, pp 593–598
23. Altintaş Y, Budak E (1995) Analytical prediction of stability lobes in milling. CIRP Ann Technol 44:357–362
24. Davies MA, Pratt JR, Dutterer B, Burns TJ (2002) Stability prediction for low radial immersion milling. J Manuf Sci Eng 124:217. https://doi.org/10.1115/1.1455030
25. Gradišek J, Govekar E, Grabec I, Kalveram M, Weinert K, Insperger T, Stépán G (2005) On stability prediction for low radial immersion milling. Mach Sci Technol 9:117–130. https://doi.org/10.1081/MST-200051378
26. Pradeep SA, Iyer RK, Kazan H, Pilla S (2017) Automotive applications of plastics: past, present, and future. Appl Plast Eng Handb:651–673. https://doi.org/10.1016/B978-0-323-39040-8.00031-6